Al/SiO₂ 芯/壳纳米结构介导飞秒激光诱导击穿机理研究

林卿[1,2*]，任乃飞[2]，宋安然[1]，夏广志[1]

[1]宿迁学院机电工程学院，江苏 宿迁 223800；

[2]江苏大学机械工程学院，江苏 镇江 212013

摘要 针对 Al/SiO₂ 芯/壳纳米结构介导飞秒激光诱导水击穿过程涉及的物理场进行了计算，在飞秒激光脉冲与纳米结构的相互作用下，纳米结构沿激光偏振方向的近场增强，造成邻域介质水出现电离击穿。对纳米尺寸下铝纳米粒子的介电函数进行了修正，利用 COMSOL 软件自带模块以及自定义方程接口，对击穿过程涉及的电磁场模型、双温模型、等离子体模型和传热模型进行了全耦合计算。主要分析了纳米粒子单体、二聚体和三聚体的近场增强，飞秒激光的击穿阈值，纳米粒子的晶格温度变化以及水等离子体的温度变化，计算结果表明，Al/SiO₂ 芯/壳纳米结构可以大幅降低飞秒激光对水的击穿阈值，聚合态纳米粒子的近场增强能力强于单体，单体的晶格温度高于熔点，二聚体和三聚体的晶格温度低于熔点。聚合态 Al/SiO₂ 芯/壳纳米结构在介导飞秒激光诱导水中空化、诱导细胞转染等应用中极具潜力。

关键词 激光技术；激光诱导击穿；铝纳米结构；相互作用机理；多物理场耦合

中图分类号 TN241　　**文献标志码** A　　　　　　　　　　**doi**：10.3788/CJL202148.1402019

1 引　　言

近年来，纳米粒子介导激光诱导光学击穿是一个活跃的研究方向，如：金纳米粒子光热疗法[1]、纳米粒子增强量子点异质结表面荧光[2]、增强拉曼散射光谱[3-4]、药物输运及靶向释放[5]、纳米粒子介导沉积基底近场微纳加工[6-8]等。激光与纳米粒子的相互作用主要包括：局部表面等离子体共振（LSPR）效应[9]，纳米粒子近场增强效应，纳米粒子尺寸、形状和分布对 LSPR 光谱特性的影响等。液体击穿时常伴随发光、空化等现象，击穿发生时，等离子体密度处于一定的范围内，即 $\rho_{crit} \approx 10^{18} \sim 10^{21}$ cm⁻³。飞秒激光击穿阈值是指形成等离子体需要达到一定电离度时对应的激光功率密度[10-14]。在纳米粒子 LSPR 导致的近场增强效应下，激光诱导纳米粒子邻域介质发生击穿。不同波长的激光可以激发纳米粒子不同强度的近场增强，这与入射激光波长是否处于纳米粒子消光截面的谐振波长附近有关。同时，不同形态的纳米粒子（如单体、聚合态等）介导下，因其近场增强能力不同，介质击穿所需的激光能量阈值也不同。

前人尝试构建了一些理论模型，并将其用于分析诱导光学击穿机理。在纳米粒子介导下，电离机理可大致分为两类：一是纳米粒子线性吸收导致的纳米粒子表面光热发射，即在飞秒激光辐照下，纳米粒子表面电子获得足够能量，产生逃逸，形成等离子体；二是纳米粒子邻域介质非线性吸收激光能量，触发多光子电离，形成等离子体[15]。Boulais 等[15]针对飞秒激光辐照金纳米粒子问题，建立了飞秒激光诱导光学击穿过程的计算模型，进一步验证了金纳米粒子邻域等离子体形成的两种不同物理机制：当激光能量密度低于 3 mJ/cm² 时，金纳米粒子直接吸收入射激光能量，光热发射成为等离子体形成的主导机理；当激光能量密

度高于 3 mJ/cm² 时,金纳米粒子邻域产生强烈的近场增强效应,多光子电离成为等离子体形成的主导机理。该模型的不足之处在于其未考虑纳米粒子介电函数的纳米尺度修正[16],当纳米粒子直径小于 150 nm 时,其光学性质会发生很大的变化[17]。Bisker 和 Yelin[18] 对不同脉宽的激光与不同尺寸的纳米粒子的相互作用进行了理论计算,但该模型未考虑等离子体与激光电磁场的双向耦合。Hatef 等[19] 模拟了飞秒激光与金纳米粒子单体、二聚体的相互作用,探讨了金纳米粒子二聚体的粒子间距对激光能量吸收的影响,但同样未考虑光学性质纳米尺度的修正。综上所述,在之前的研究中,缺乏对激光诱导击穿涉及的电磁场、等离子体场、双温模型和传热模型等四个物理模型的全耦合计算,同时缺乏对纳米尺度下纳米粒子介电函数的修正。

在现有研究中,金纳米粒子以其良好性能成为研究热点。近期,Liu 等[20] 报道了聚合态金纳米粒子在增强激光诱导击穿光谱以及在提高污水重金属离子检测方面的应用。Simakin 等[21] 报道了水溶液中金纳米粒子的浓度对激光诱导水电离击穿的影响。Koral 等[22] 将金纳米粒子应用于透明样品,避免了激光对透明样品进行光谱检测时造成的损伤。铝纳米粒子作为一种新型材料,近年来已出现较多相关的应用研究。铝纳米粒子比金、银等贵金属纳米粒子廉价易得,但其在水和空气中性质活泼;石英玻璃可用作铝芯的保护层且不影响铝芯的光学性能。美国 NANOSHEL 公司已于 2016 年成功制备了多种规格的 Al/SiO₂ 芯/壳结构纳米粒子,铝芯中铝元素的质量分数高达 99.9%,SiO₂ 壳厚为 10~15 nm。Al/SiO₂ 芯/壳结构纳米粒子已成功应用于如光纤、热核装置、温度传感器、超高真空装置等[23],本文利用 COMSOL 软件耦合计算了 Al/SiO₂ 芯/壳结构纳米粒子介导下,飞秒激光诱导介质环境(水)发生光学击穿时涉及的多个物理场,并对其机理做了进一步探讨。

2 多物理场耦合计算方法

2.1 电磁场模型

如图 1(a) 所示,最外层为入射激光电磁场求解域的理想匹配层(PML),用于设定电磁场的有限计算区域,截断电磁场的边界反射。最内层和中间层均表示环境介质水,其中最内层用于计算等离子体电子密度的变化过程。中心圆点处灰色和白色的部分分别表示 Al/SiO₂ 芯/壳纳米粒子的 Al 芯和 SiO₂ 壳。入射激光电场的偏振方向为 Z 轴方向,传播方向为 Y 轴正方向。Al/SiO₂ 芯/壳纳米粒子结构如图 1(b) 所示,d 为 Al 芯直径,d_s 为 SiO₂ 壳厚,d_g 为聚合态纳米粒子间隙。为了与无纳米粒子介导时纯水的飞秒激光电离阈值进行比较,将本算例中入射激光的波长 λ 设为 580 nm,脉冲激光脉宽 t_p 设为 300 fs,激光参数与无纳米粒子介导下的激光参数保持一致。根据美国 NANOSELL 公司研发的 Al/SiO₂ 芯/壳结构纳米粒子尺寸的相关报道[23],可知纳米粒子的平均直径为 80~100 nm(含 SiO₂ 壳厚 10 nm),其中直径为 100 nm 的粒子占比为 60%,占比最高,且相对于直径<100 nm 规格的纳米粒子而言,具有更强的近场增强效应。所以本文选此规格进行计算,同时可为以后实验研究中实验参数(如飞秒激光击穿能量阈值等)的设定提供依据。将本算例中铝芯直径 d 设定为 80 nm,SiO₂ 壳厚度 d_s 设定为 10 nm,粒子间隙 d_g 设定为 2 nm。

近场电场 $\boldsymbol{E}$ 可由亥姆霍兹波动方程计算得出。亥姆霍兹波动方程为

$$\boldsymbol{E}(x,y,z) = \boldsymbol{E}_0 \frac{w_0}{w(y)} \exp \times$$
$$\left[-\frac{z^2+x^2}{w^2(y)} - \mathrm{j}ky - \mathrm{j}k\frac{z^2+x^2}{2R(y)} + \mathrm{j}\eta(y) \right], \quad (1)$$
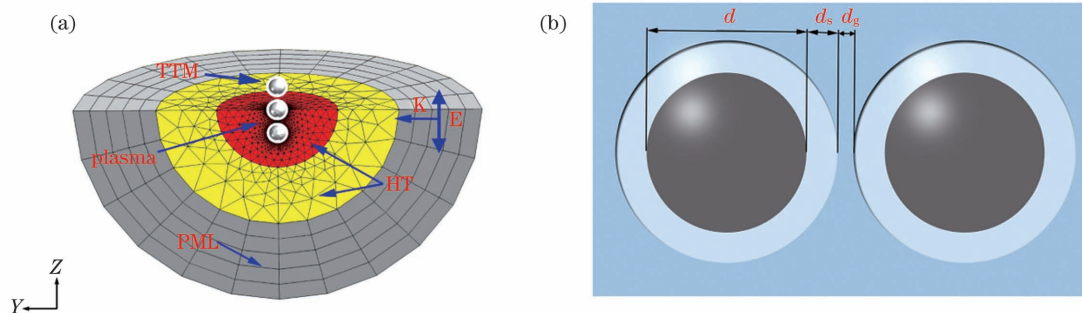$$\nabla \times (\nabla \times \boldsymbol{E}) - k_0^2 \varepsilon \boldsymbol{E} = 0, \quad (2)$$

(a)

(b)

图 1 Al/SiO₂ 芯/壳纳米结构及其网格化。(a) 网格结构;(b) Al/SiO₂ 芯/壳纳米结构

Fig. 1 Al/SiO₂ core/shell nanostructure and its meshing. (a) Mesh structure; (b) Al/SiO₂ core-shell nanostructure

式中：$\boldsymbol{E}_0$ 为入射激光电场，入射激光电场强度 $E_0 = \sqrt{2I_{in}/(c_0 n\varepsilon_0)}$，$n$ 为介质折射率，c_0 为真空光速，ε_0 为真空介电常数，I_{in} 为入射激光强度，$I_{in} = J \cdot f(t_p)/t_p$，$J$ 为激光能量密度，t_p 为激光脉宽，$f(t_p)$ 为激光脉冲在时间尺度上的高斯分布；k 为波数，k_0 为真空波数，$k_0 = k/n$；ε 为复相对介电常数；w_0 为最小束腰半径；$w(y) = w_0\sqrt{1+\left(\dfrac{y}{y_0}\right)^2}$，$R(y) = y\left[1+\left(\dfrac{y_0}{y}\right)^2\right]$，$\eta(y) = \arctan\left(\dfrac{y}{y_0}\right)$，其中 y_0 为瑞利长度，$y_0 = \dfrac{k_0 w_0^2}{2}$。其余参数见表 1。

表 1 多物理场耦合模型中所用参数

Table 1 Parameters used in multi-physical fields coupling model

Parameter	Value	Description
λ /nm	580	Laser wavelength
$c_0/(\mathrm{m \cdot s^{-1}})$	3×10^8	Speed of light in vacuum
ω	$2\pi c_0/\lambda$	Angular frequency
$\varepsilon_0/(\mathrm{F \cdot m^{-1}})$	8.85×10^{-12}	Vacuum permittivity
t_p/fs	300	Laser pulse width [full width at half maximum (FWHM)]
e /C	1.6×10^{-19}	Electron charge
m_w/kg	3×10^{-26}	Mass of water molecule
m_s/kg	9.9765×10^{-26}	Mass of silica molecule
m_e/kg	$9.10938291 \times 10^{-31}$	Electron mass
m'_s	$0.86 m_e$	Effective silica electron mass[24]
m'_w	$0.5 m_e$	Effective water electron mass[12,14]
τ /fs	1.6	Mean free time between electron/molecule collisions[25]
$\hbar/(\mathrm{J \cdot s})$	$1.0545718 \times 10^{-34}$	Reduced Planck constant
$E_{w,gap}$/eV	6.5	Band gap energy of water[26]
$E_{s,gap}$/eV	9	Band gap energy of silica[27]
$\rho_{w,bound}/\mathrm{cm^{-3}}$	6.68×10^{22}	Bound electron density of water[12]
$\rho_{s,bound}/\mathrm{cm^{-3}}$	2.2×10^{22}	Bound electron density of silica[27]
n_w	1.33	Refractive index of water
n_s	1.45	Refractive index of silica
$\eta_{rec}/(\mathrm{cm^3 \cdot s^{-1}})$	2×10^{-9}	Empirical recombination rate[28]
$q_0/(\mathrm{W \cdot m^{-2} \cdot K^{-1}})$	133.4×10^6	Thermal conductance at aluminum-silica interface[29]
$q_1/(\mathrm{W \cdot m^{-2} \cdot K^{-1}})$	1000×10^6	Thermal conductance at silica-water interface[30]
$\rho_s/(\mathrm{kg \cdot m^{-3}})$	2203	Density of silica
$\rho_w/(\mathrm{kg \cdot m^{-3}})$	1000	Density of water
$c_s/(\mathrm{J \cdot kg^{-1} \cdot K^{-1}})$	703	Heat capacity of silica
$c_w/(\mathrm{J \cdot kg^{-1} \cdot K^{-1}})$	4184	Heat capacity of water
$k_s/(\mathrm{W \cdot m^{-1} \cdot K^{-1}})$	1.38	Thermal conductivity of silica
$k_w/(\mathrm{W \cdot m^{-1} \cdot K^{-1}})$	0.61	Thermal conductivity of water

对纳米粒子来说，当其直径小于 150 nm 时，常规介电函数已不能准确适用，因此，需对常规介电函数进行纳米尺寸修正。铝的常规介电函数可利用临界点模型（CPM）表述，表达式为[31]

$$\varepsilon_{CPM}(\omega) = \varepsilon_\infty - \frac{\omega_p^2}{\omega(\omega + \mathrm{j}\gamma_D)} + \sum_{p=1}^{2} A_p \Omega_p \left[\frac{\exp(\mathrm{j}\varphi_p)}{\Omega_p - \omega - \mathrm{j}\Gamma_p} + \frac{\exp(-\mathrm{j}\varphi_p)}{\Omega_p + \omega + \mathrm{j}\Gamma_p}\right], \quad (3)$$

式中:ε_∞ 为介电常数;ω_p 为等离子频率;ω 为激光频率;γ_D 为阻尼系数;A_p 为权重因数;Ω、ϕ 和 Γ 分别为能隙、相位和展宽。文献[32]的各项参数值选取如下:$\varepsilon_\infty = 1$,$\omega_p = 2.0598 \times 10^{16}$ Hz,$\gamma_D = 2.2876 \times 10^{14}$ Hz,$A_1 = 5.2306$,$\phi_1 = -0.51202$,$\Omega_1 = 2.2694 \times 10^{15}$ Hz,$\Gamma_1 = 3.2867 \times 10^{14}$ Hz,$A_2 = 5.2704$,$\phi_2 = 0.42503$,$\Omega_2 = 2.4668 \times 10^{15}$ Hz,$\Gamma_2 = 1.7731 \times 10^{15}$ Hz。

考虑到铝纳米粒子的尺寸效应,参照金纳米粒子介电函数的修正方法[16],直径小于 150 nm 的铝纳米粒子介电函数的修正函数为

$$\varepsilon(\omega, L_{\mathrm{eff}}) = \varepsilon_{\mathrm{CPM}}(\omega) + \frac{\omega_p^2}{\omega(\omega + \mathrm{j}\Gamma_{\mathrm{bulk}})} - \frac{\omega_p^2}{\omega^2 + \mathrm{j}\omega\left(\Gamma_{\mathrm{bulk}} + \frac{A v_{\mathrm{F}}}{L_{\mathrm{eff}}} + \frac{\hbar \eta V_{\mathrm{np}}}{\pi}\right)}, \quad (4)$$

式中:L_{eff} 为有效平均自由程,$L_{\mathrm{eff}} = 4V_{\mathrm{np}}/S_{\mathrm{np}}$,$V_{\mathrm{np}}$ 为纳米粒子体积;Γ_{bulk} 为纳米粒子的阻尼常数,$\Gamma_{\mathrm{bulk}} = v_{\mathrm{F}}/l_\infty$,其中 $v_{\mathrm{F}} = 2.02$ nm/fs 为费米速度,$l_\infty = 16$ nm 为电子碰撞平均自由程[17];A 为表面约束展宽系数,$A = \Gamma_{\mathrm{surf}} L_{\mathrm{eff}}/v_{\mathrm{F}}$,其中 Γ_{surf} 为纳米粒子表面电子碰撞和散射阻尼常数,根据文献[16]假设 $A = 0.5$;Γ_{rad} 为辐射阻尼常数,$\Gamma_{\mathrm{rad}} = \hbar \eta V_{\mathrm{np}}/\pi$,其中 $\hbar$ 为约化普朗克常数,$\hbar = 1.0545718 \times 10^{-34}$ J·s,η 为铝纳米粒子辐射阻尼系数。因缺乏小尺寸(<150 nm)铝纳米粒子辐射阻尼系数 η 的准确数值,参照金纳米粒子的研究结果,对 Novo 等[33]和 Sönnichsen 等[34]的实验结果取平均值,即 $\eta = (5.5 \pm 1.5) \times 10^{-7}$ fs^{-1}·nm^{-3},该数值与银纳米粒子的相关研究结果[35]一致,因此该数值有可能适用于其他金属纳米粒子[33]。

使用 Drude 模型来描述纳米粒子邻域环境介质介电函数的变化,表达式为[36]

$$\varepsilon_{\mathrm{w}} = \varepsilon_{\mathrm{r}} - \frac{\rho_{\mathrm{e}} e^2}{\varepsilon_0 m'(\omega^2 + \mathrm{j}\omega/\tau)}, \quad (5)$$

其中 ε_{r} 为环境介质的相对介电常数,m' 为有效电子质量,τ 为电子/分子碰撞的平均自由时间,ρ_{e} 为等离子体电子密度。

2.2 双温模型

利用双温模型计算铝芯电子温度 T_{e} 和晶格温度 T_1。双温模型与电磁场模型之间利用电磁场中铝芯的阻抗损耗 Q_{rh} 进行耦合[37]。耦合计算方程为

$$C_{\mathrm{e}} \frac{\partial T_{\mathrm{e}}}{\partial t} = -G(T_{\mathrm{e}} - T_1) + Q_{\mathrm{rh}} \cdot f(t_{\mathrm{p}}), \quad (6)$$

$$C_1 \frac{\partial T_1}{\partial t} = G(T_{\mathrm{e}} - T_1), \quad (7)$$

$$Q_{\mathrm{rh}} = \frac{1}{2} \mathrm{Re}\left[(\sigma - \mathrm{j}\omega\varepsilon) \boldsymbol{E} \cdot \boldsymbol{E}^*\right], \quad (8)$$

式中 C_{e} 为铝芯电子热容[38],C_1 为铝芯晶格热容[39],G 为电子-声子耦合系数[38],$\mathrm{Re}[\cdot]$ 表示取实部运算,σ 为电导率。

2.3 等离子体模型

2.3.1 等离子体速率方程

等离子体电子密度速率方程的一般形式可以表示为[11]

$$\frac{\mathrm{d}\rho_{\mathrm{e}}}{\mathrm{d}t} = \left(\frac{\mathrm{d}\rho_{\mathrm{e}}}{\mathrm{d}t}\right)_{\mathrm{photo}} + \left(\frac{\mathrm{d}\rho_{\mathrm{e}}}{\mathrm{d}t}\right)_{\mathrm{casc}} + \left(\frac{\mathrm{d}\rho_{\mathrm{e}}}{\mathrm{d}t}\right)_{\mathrm{diff}} + \left(\frac{\mathrm{d}\rho_{\mathrm{e}}}{\mathrm{d}t}\right)_{\mathrm{rec}}, \quad (9)$$

式中:$\left(\dfrac{\mathrm{d}\rho_{\mathrm{e}}}{\mathrm{d}t}\right)_{\mathrm{photo}}$ 为光致电离速率方程[40],主导机理为多光子吸收和隧穿电离;$\left(\dfrac{\mathrm{d}\rho_{\mathrm{e}}}{\mathrm{d}t}\right)_{\mathrm{casc}}$ 为雪崩电离速率方程[41],主导机理为逆韧致辐射吸收和碰撞电离;$\left(\dfrac{\mathrm{d}\rho_{\mathrm{e}}}{\mathrm{d}t}\right)_{\mathrm{diff}} = \dfrac{-2\tau(5/4)\widetilde{\Delta}}{3m_{\mathrm{e}}\Lambda^2}\rho_{\mathrm{e}}$,为等离子体电子扩散速率方程,其中 m_{e} 为电子质量,Λ 为特征扩散长度,设定为纳米粒子半径。$\widetilde{\Delta}$ 为有效电离势[25];$\left(\dfrac{\mathrm{d}\rho_{\mathrm{e}}}{\mathrm{d}t}\right)_{\mathrm{rec}} = -\eta_{\mathrm{rec}}\rho_{\mathrm{e}}^2$,为等离子体电子复合速率方程,其中 η_{rec} 为经验重组率[28]。

2.3.2 光致电离

光致电离速率方程为[25]

$$\left(\frac{\mathrm{d}\rho_{\mathrm{e}}}{\mathrm{d}t}\right)_{\mathrm{photo}} = \frac{2\omega}{9\pi}\left(\frac{m'\omega\sqrt{1+\gamma^2}}{\hbar\gamma}\right)^{3/2} Q\left(\gamma, \frac{\widetilde{\Delta}}{\hbar\omega}\right) \times \left(\frac{\rho_{\mathrm{bound}} - \rho_{\mathrm{e}}}{\rho_{\mathrm{bound}}}\right) \times$$

$$\exp\left\{-\pi\left\langle\frac{\widetilde{\Delta}}{\hbar\omega}+1\right\rangle \times \left[\kappa\left(\frac{\gamma}{\sqrt{1+\gamma^2}}\right) - \varepsilon\left(\frac{\gamma}{\sqrt{1+\gamma^2}}\right)\right]\Big/\varepsilon\left(\frac{1}{\sqrt{1+\gamma^2}}\right)\right\}, \quad (10)$$

式中:γ 为 Keldysh 系数[40],$\gamma = \omega \dfrac{\sqrt{m'E_{\mathrm{gap}}}}{e|\boldsymbol{E}|}$,$E_{\mathrm{gap}}$ 为介质能带隙,e 为电子电荷;$Q\left(\gamma, \dfrac{\widetilde{\Delta}}{\hbar\omega}\right)$ 为与 γ 和 $\widetilde{\Delta}$ 有

关的函数。由于纳米粒子近场的增强效应,Keldysh 系数 γ 的计算应基于增强后的电场幅值来计算。

2.3.3 雪崩电离

光致电离所致电子密度达到临界电子密度 ρ_{seed} 时发生雪崩电离,种子电子临界电子密度[42]的表达式为 $\rho_{\mathrm{seed}}=10^{-0.01116\ \mathrm{nm}^{-1}\cdot\lambda+23.5}\ \mathrm{cm}^{-3}$。其中单个电子的雪崩电离速率方程为[12]

$$\eta_{\mathrm{casc}}=\frac{1}{\omega^2\tau^2+1}\left[\frac{e^2\tau}{c_0 n\varepsilon_0 m_{\mathrm{e}}(3/2)\widetilde{\Delta}}I_{\mathrm{in}}(t)-\frac{m_{\mathrm{e}}\omega^2\tau}{M}\right], \tag{11}$$

其中,M 为分子质量。雪崩电离速率方程为[25]

$$\left(\frac{\mathrm{d}\rho_{\mathrm{e}}}{\mathrm{d}t}\right)_{\mathrm{casc}}=$$

$$\begin{cases}\dfrac{\rho_{\mathrm{e}}}{1+\eta_{\mathrm{casc}}t_{\mathrm{ret}}}\left[\alpha_{\mathrm{casc}}I_{\mathrm{in}}(t)-\beta_{\mathrm{casc}}\right], & \rho_{\mathrm{e}}\geqslant\rho_{\mathrm{seed}}\\ 0, & \rho_{\mathrm{e}}<\rho_{\mathrm{seed}}\end{cases}, \tag{12}$$

式中:α_{casc} 为级联电离增益[25],β_{casc} 为级联电离碰撞损耗[25],t_{ret} 为延迟时间[25]。

2.4 传热模型

基于传热模型,计算了飞秒激光作用下纳米粒子 Al 芯-SiO$_2$-水的热扩散和等离子体吸热引起的急剧温升。综合考虑 4 种热源项:1)Al 芯晶格-SiO$_2$ 壳传热时的边界热通量 $Q_{\mathrm{np|s}}=q_0(T_1-T_{\mathrm{s}})$ 及 SiO$_2$ 壳-水传热时的边界热通量 $Q_{\mathrm{s|w}}=q_1(T_{\mathrm{s}}-T_{\mathrm{w}})$,其中 q_0 为纳米铝芯-SiO$_2$ 壳界面对流换热系数,q_1 为 SiO$_2$ 壳-水界面对流换热系数,T_{s} 和 T_{w} 为 SiO$_2$ 壳晶格和水等离子体的温度;2)Al 芯在激光入射电场中的阻抗损耗热源项 Q_{rh},即 $\rho_{\mathrm{s}}c_{\mathrm{s}}\dfrac{\partial T_{\mathrm{s}}}{\partial t}=\nabla(k_{\mathrm{s}}\nabla T_{\mathrm{s}})+Q_{\mathrm{rh}}\cdot f(t_{\mathrm{p}})$,其中 ρ_{s} 为 SiO$_2$ 密度,c_{s} 为 SiO$_2$ 的比热容,k_{s} 为 SiO$_2$ 的热导率;3)等离子体电子碰撞损耗热源项 $\left(\dfrac{\mathrm{d}T_{\mathrm{w}}}{\mathrm{d}t}\right)_{\mathrm{coll}}=\dfrac{5}{4c_{\mathrm{w}}\rho_{\mathrm{w}}}E_{\mathrm{gap}}\beta_{\mathrm{casc}}\rho_{\mathrm{e}}$,其中 c_{w} 为水的比热容,ρ_{w} 为水的密度;4)等离子体电子复合热源项 $\left(\dfrac{\mathrm{d}T_{\mathrm{w}}}{\mathrm{d}t}\right)_{\mathrm{rec}}=\dfrac{5}{4c_{\mathrm{w}}\rho_{\mathrm{w}}}E_{\mathrm{gap}}\eta_{\mathrm{rec}}\rho_{\mathrm{e}}^2$。水等离子体的传热方程为

$$\rho_{\mathrm{w}}c_{\mathrm{w}}\frac{\partial T_{\mathrm{w}}}{\partial t}=\nabla(k_{\mathrm{w}}\nabla T_{\mathrm{w}})+\left(\frac{\mathrm{d}T_{\mathrm{w}}}{\mathrm{d}t}\right)_{\mathrm{coll}}+\left(\frac{\mathrm{d}T_{\mathrm{w}}}{\mathrm{d}t}\right)_{\mathrm{rec}}, \tag{13}$$

其中 k_{w} 为水的热导率。

2.5 多物理场模型耦合

四个物理场的耦合关系如图 2 所示,EM 为电

磁场物理场,TTM 为双温模型物理场,HT 为传热物理场,plasma 为等离子体物理场。EM 与 TTM 和 HT 为单向耦合;TTM 与 plasma,plasma 与 HT 为单向耦合;EM 与 plasma 为双向耦合;TTM 与 HT 为双向耦合。利用 COMSOL 强大的多物理场耦合计算能力,对四个物理场同时进行了计算。EM 和 HT 采用 COMSOL 内置模块进行模拟,TTM 和 PLASMA 则利用自定义方程(PDE)接口,将相关物理场方程写入 COMSOL 进行耦合,耦合参数及其计算方程如图 2 所示。
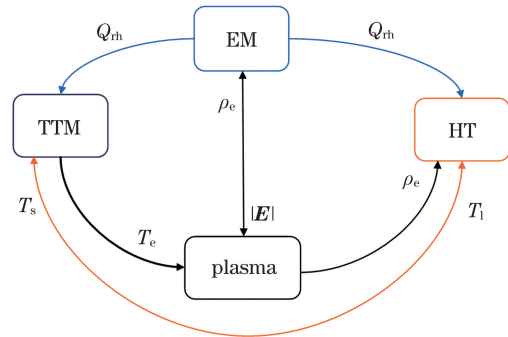

图 2 耦合流程图

Fig. 2 Coupling flow chart

3 计算结果分析与讨论

在实际应用中,常常将纳米粒子沉积于基底上,所以本算例中,分别计算了 Al/SiO$_2$ 芯/壳纳米粒子单体、二聚体和三聚体沉积于石英(SiO$_2$)基底上的近场增强,飞秒激光对邻近水域的击穿阈值,Al 芯晶格温度和水域等离子体电子密度的变化过程等。纳米粒子单体几何模型如图 3 所示,其中双温模型的计算域仅限于 Al 芯,用于计算其电子与晶格温度的变化,等离子体模型的计算域为 SiO$_2$ 壳、基底及邻近水域,用于计算等离子体电子密度的变化及等离子体温度的变化。
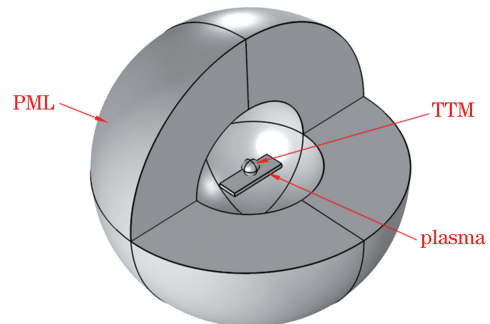
水中不同形态 Al/SiO$_2$ 芯/壳纳米粒子的相对电

图 3 单体计算模型

Fig. 3 Calculation model of monomer

场增强因子 $\xi=|\boldsymbol{E}|/E_0$ 如图 4 所示,其中 $|\boldsymbol{E}|$ 为电场幅值,E_0 为入射激光电场强度。单体的最大电场增强因子为 2.23,最大电场位于单体两侧,沿入射激光电场的偏振方向(Z 轴),如图 4(a)所示。二聚体、三聚体的最大相对电场增强因子分别为 4.23 和 4.38,最大电场位于纳米粒子间隙,沿入射激光电场的偏振方向,如图 4(b)、图 4(c)所示。沿 Z 轴方向纳米结构中心线处的相对电场增强因子如图 5(b)所示,因单体、二聚体和三聚体纳米结构及其电场分布

在 XZ 平面关于 $Z=0$ 轴对称,故仅列出 $Z=-160\sim 0$ nm 范围内的电场数值。单体和三聚体在 $Z=-40$ nm 处取得最大值,二聚体在 $Z=-11$ nm 处取得最大值,即沿 Z 轴方向,三种纳米结构均在 Al 芯表面取得电场最大值,但二聚体的最大电场位于两粒子之间的 Al 芯表面,而三聚体的最大电场位于正中间粒子的 Al 芯表面。二聚体、三聚体相对于单体而言,最大电场增强因子提高近一倍,说明聚合态 Al/SiO_2 芯/壳纳米粒子的近场增强能力较强。
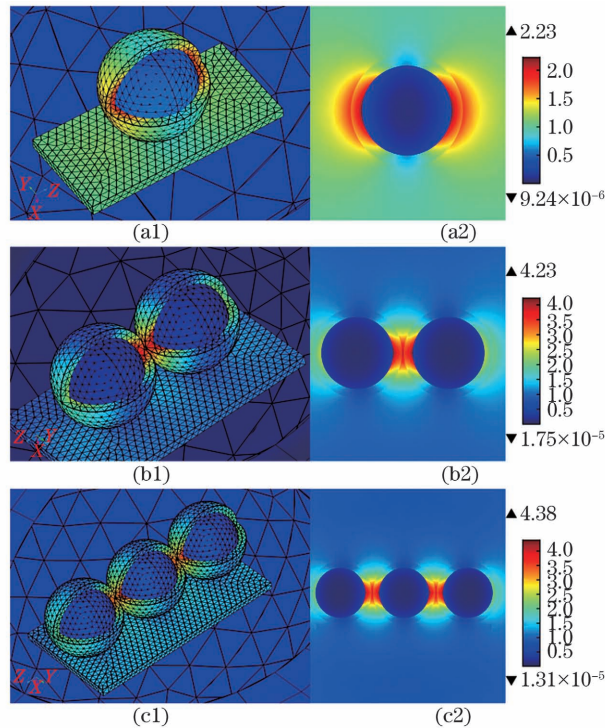
图 4 水中不同形态下 Al/SiO_2 芯/壳纳米粒子的相对电场增强因子 ξ。(a1)(a2)单体及其 XZ 截面;(b1)(b2)二聚体及其 XZ 截面;(c1)(c2)三聚体及其 XZ 截面

Fig. 4 Relative enhancement factor of electric field ξ for different morphology of Al/SiO_2 core/shell nanoparticles in water. (a1)(a2) Monomer and its XZ cross section; (b1)(b2) dimer and its XZ cross section; (c1)(c2) trimer and its XZ cross section
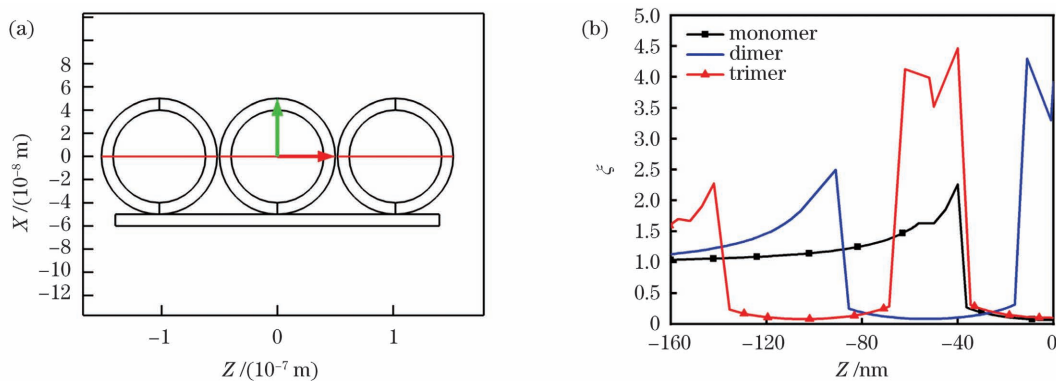

图 5 纳米结构及其沿 Z 轴方向纳米结构中心线处的相对电场增强因子。(a)纳米结构;(b)沿 Z 轴方向纳米结构中心线处的相对电场增强因子

Fig. 5 Proposed nanostructure and relative enhancement factor of electric field ξ at the center line of the nanostructure along Z-axis. (a) Proposed nanostructure; (b) relative enhancement factor of electric field ξ

单体、二聚体和三聚体的 Al/SiO_2 芯/壳纳米粒子在入射波长为 200~600 nm 的消光截面如图 6 所示,其中三聚体在入射波长为 230 nm 时,消光截面达到峰值 16735 nm^2;二聚体在入射波长为 200 nm 时,消光截面达到峰值 4433 nm^2;单体在入射波长为 230 nm 时,消光截面达到峰值 2734 nm^2。此外,入射波长 $\lambda=580$ nm 时三聚体、二聚体和单体的消光截面分别为 4115,209,74 nm^2,均处于非谐振态。
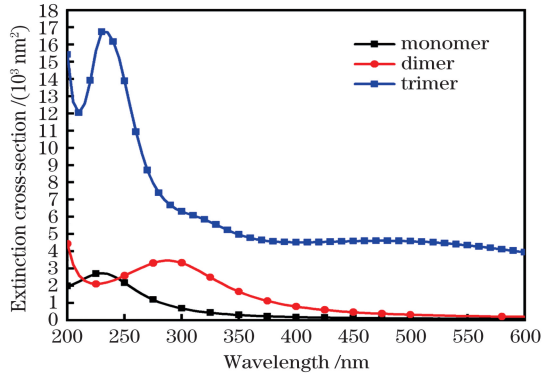

图 6 Al/SiO_2 芯/壳纳米粒子单体、二聚体和三聚体的消光截面

Fig. 6 Extinction cross-section for monomer, dimer and trimer of Al/SiO_2 core/shell nanoparticles

不同形态的纳米粒子在一个脉冲周期内($4t_p$)的电子密度变化过程如图 7 所示,图中:水平虚线 1(下方)表示水发生电离时等离子体电子密度需要达到的阈值[43],即 $\rho_e=1.8\times10^{20}$ cm^{-3},而 SiO_2 发生

电离时等离子体电子密度需要达到的阈值在 1×10^{20}~3×10^{20} cm^{-3} 之间[44];水平虚线 2(上方)表示当水和 SiO_2 壳均发生电离时,纳米粒子邻域水域中的等离子体电子密度达到的上限阈值,即纳米粒子邻域等离子体电子密度达到饱和状态时的电子密度阈值,即 $\rho_e=3\times10^{20}$ cm^{-3}。

单体介导下,如图 7(a)所示,在激光能量密度 $J=158$ mJ/cm^2 辐照下,水的电子密度变化过程如图中三角曲线所示,在 $t=790$ fs 时达到击穿电子密度阈值(1.8×10^{20} cm^{-3}),未达到饱和电子密度阈值(3×10^{20} cm^{-3});当入射激光能量密度提高到 173 mJ/cm^2 时,在 $t=780$ fs 时达到饱和电子密度阈值;当激光能量继续提高至 220 mJ/cm^2 时,在 $t=485$ fs 时达到击穿电子密度阈值,在 $t=535$ fs 时达到饱和电子密度阈值。二聚体介导下,如图 7(b)所示,在 $J=37$ mJ/cm^2 时,在 $t=780$ fs 时达到击穿电子密度阈值;在 $J=40$ mJ/cm^2 时,在 $t=750$ fs 时达到饱和电子密度阈值;在 $J=60$ mJ/cm^2 时,在 $t=390$ fs 时达到击穿电子密度阈值,在 $t=425$ fs 时达到饱和电子密度阈值。三聚体介导下,如图 7(c)所示,在 $J=36$ mJ/cm^2 时,在 $t=780$ fs 时达到击穿电子密度阈值;在 $J=39$ mJ/cm^2 时,在 $t=750$ fs 时达到饱和电子密度阈值;在 $J=50$ mJ/cm^2 时,在 $t=495$ fs 时达到击穿电子密度阈值,在 $t=552$ fs 时达到饱和电子密度阈值。对比发现,聚合态 Al/SiO_2 芯/壳纳米粒子介导时,各自的
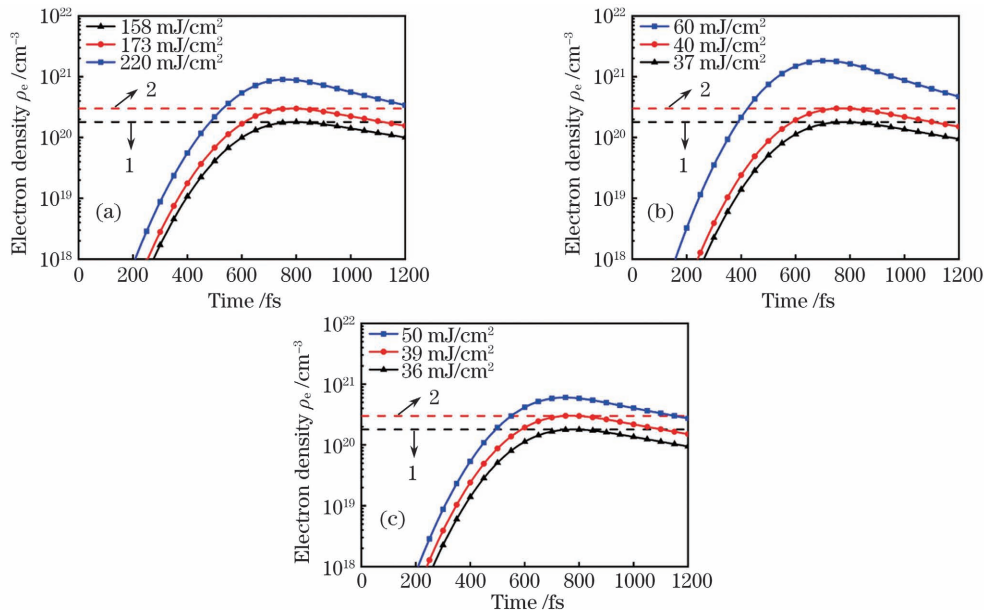

图 7 不同形态 Al/SiO_2 芯/壳纳米粒子介导下的等离子体电子密度变化过程。(a)单体;(b)二聚体;(c)三聚体

Fig. 7 Evolution of plasma electron density for different morphology of Al/SiO_2 core/shell nanoparticles. (a) Monomer; (b) dimer; (c) trimer

激光击穿能量阈值下,等离子体电子达到击穿电子密度阈值和饱和电子阈值的时间相同。从单体、二聚体到三聚体,等离子体电子达到击穿密度阈值时所需的激光功率密度逐渐减小,这归因于纳米粒子的近场增强能力不断增强。在无纳米粒子介导下,同样参数(波长、脉宽)的飞秒激光对纯水的击穿阈值[45]为 1428 mJ/cm²,这说明 Al/SiO₂ 芯/壳纳米结构可大幅降低所需的激光强度。

在一个激光脉冲作用周期结束时,即 $t=1200$ fs 时单体、二聚体和三聚体 Al/SiO₂ 芯/壳纳

米粒子介导下,不同各自激光击穿能量阈值对应的晶格温度分别如图 8(a)～(c)所示:单体的最大温度为 961 K,处于入射激光束的迎向面;二聚体的最大温度为 604 K,分布于入射激光束的迎向面,并向近场增强位置(粒子间隙处)倾斜;三聚体的最大温度为 655 K,处于入射激光束的迎向面,位于正中间纳米粒子上,上下两个纳米粒子的最大温度分布向近场增强位置倾斜,与二聚体类似。所以,单体、二聚体和三聚体的最大温度位置是入射激光与粒子间近场增强耦合作用的结果。
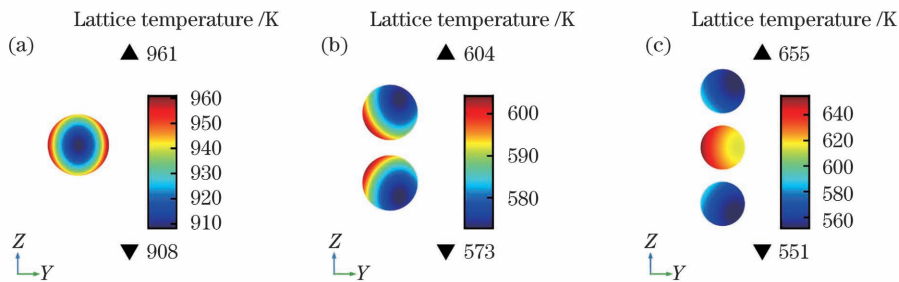

图 8 $t=1200$ fs 时不同形态 Al/SiO₂ 芯/壳纳米粒子在对应激光击穿能量下的晶格温度。(a)单体;(b)二聚体;(c)三聚体

Fig. 8 Lattice temperature of different morphology of Al/SiO₂ core/shell nanoparticles at corresponding laser breakdown fluence at $t=1200$ fs. (a) Monomer; (b) dimer; (c) trimer

单体、二聚体和三聚体的 Al/SiO₂ 芯/壳纳米粒子,在各自水域中电子达到饱和电子密度对应的激光击穿能量密度下,晶格温度在 8 ps 时间内的变化过程如图 9 所示,单体在 $J=173$ mJ/cm² 下的稳态晶格温度为 1584 K,三聚体在 $J=39$ mJ/cm² 下的稳态晶格温度为 799 K,二聚体在 $J=40$ mJ/cm² 时的稳态晶格温度为 718 K,其中二聚体和三聚体的稳态晶格温度未达到铝芯熔点,但是三聚体在较低的激光能量密度下获得了比二聚体在较高激光能

量密度下更大的稳态温度,这是因为晶格温度是由电磁场的阻抗损耗决定的,而阻抗损耗又是由纳米粒子邻域获得近场增强后的电场幅值决定的。三聚体相比二聚体,近场增强能力更强。

当激光能量密度提高到击穿能量阈值时,环境介质水在一个脉冲周期($4t_p$)内即可发生电离击穿(如图 7 所示)。以三聚体介导为例,纳米粒子邻域水等离子体电子的温度变化如图 10 所示,随着电离击穿的发生,等离子体急剧吸收激光能量,温度迅速升高,在 $t=850$ fs 时达到峰值 11937 K。

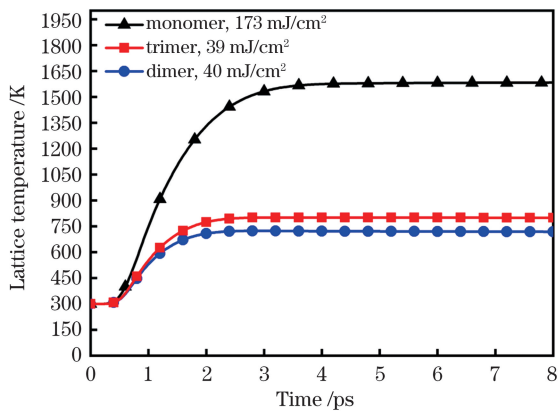图 9 不同形态 Al/SiO₂ 芯/壳纳米粒子的晶格温度变化过程

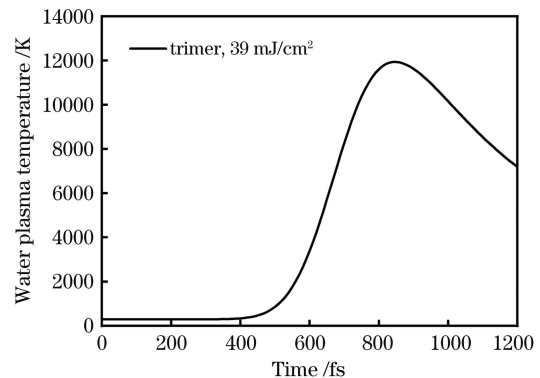Fig. 9 Evolution of lattice temperature of different morphology of Al/SiO₂ core/shell nanoparticles

图 10 三聚体介导下水等离子体的电子温度变化

Fig. 10 Evolution of electron temperature of water plasma mediated by trimer

4 结 论

通过对单脉冲飞秒激光与 Al/SiO_2 芯/壳纳米结构及其介质环境水相互作用过程中涉及的电磁场、等离子体场、传热场和双温模型等多个物理场进行全耦合计算，发现单体、二聚体和三聚体的近场增强能力逐渐增强，介导介质环境水电离击穿时，三聚体所需的激光能量密度最小，这归因于其近场增强能力最强。在不同激光诱导介质环境水的击穿阈值下，不论是在一个脉冲周期作用结束时，还是纳米粒子晶格温度达到稳态时，单体的晶格温度均最高。理论计算表明，聚合态 Al/SiO_2 芯/壳纳米结构可大幅降低飞秒激光对水的击穿阈值，由此说明聚合态 Al/SiO_2 芯/壳纳米结构在介导水中空化、细胞转染等应用中具有较大前景。

参 考 文 献

[1] Ren Y T, Qi H, Chen Q, et al. Thermal dosage investigation for optimal temperature distribution in gold nanoparticle enhanced photothermal therapy[J]. International Journal of Heat and Mass Transfer, 2017, 106: 212-221.

[2] Liu P C, Chang M Y, Bai Z C, et al. Enhanced fluorescence of $CdSe/Al_2O_3$ heterojunctions enabled by TiN nanoparticles[J]. Chinese Journal of Lasers, 2020, 47(9): 0913001.
刘鹏程，昌梦雨，白忠臣，等. TiN 纳米粒子增强 $CdSe/Al_2O_3$ 异质结荧光的研究[J]. 中国激光，2020, 47(9): 0913001.

[3] Xin K, Shi X F, Zhang X, et al. Aggregation of gold nanoparticles based on photothermal effect and its application in surface-enhanced Raman scattering[J]. Acta Optica Sinica, 2020, 40(19): 0193001.
辛坤，史晓凤，张旭，等. 基于光热效应实现金纳米粒子的聚集及其 SERS 应用[J]. 光学学报，2020, 40(19): 0193001.

[4] Zhang X L, Zhang J, Zhu Y. Microfluidic surface-enhanced Raman scattering experiment using CNTs/AgNPs composite structure[J]. Chinese Journal of Lasers, 2019, 46(10): 1011001.
张晓蕾，张洁，朱永. CNTs/AgNPs 复合结构的微流控表面增强拉曼散射实验[J]. 中国激光，2019, 46(10): 1011001.

[5] Lukianova-Hleb E Y, Belyanin A, Kashinath S, et al. Plasmonic nanobubble-enhanced endosomal escape processes for selective and guided intracellular delivery of chemotherapy to drug-resistant cancer cells[J]. Biomaterials, 2012, 33(6): 1821-1826.

[6] Terakawa M, Mitsuhashi T, Shinohara T, et al. Near-infrared femtosecond laser-triggered nanoperforation of hollow microcapsules[J]. Optics Express, 2013, 21(10): 12604-12610.

[7] Bityurin N M, Afanasiev A V, Bredikhin V I, et al. Surface nanostructuring by bichromatic femtosecond laser pulses through a colloidal particle array[J]. Quantum Electronics, 2014, 44(6): 556-562.

[8] Tanaka Y, Obara G, Zenidaka A, et al. Femtosecond laser near-field nanoablation patterning using Mie resonance high dielectric constant particle with small size parameter[J]. Applied Physics Letters, 2010, 96(26): 261103.

[9] Wang S, Zhang H, Li W, et al. Construction and experimental study of a multi-channel localized surface plasmon resonance analysis device[J]. Acta Optica Sinica, 2019, 39(2): 0228002.
王顺，张浩，李伟，等. 多通道局域表面等离子体共振分析装置构建及实验研究[J]. 光学学报，2019, 39(2): 0228002.

[10] Bloembergen N. Laser-induced electric breakdown in solids[J]. IEEE Journal of Quantum Electronics, 1974, 10(3): 375-386.

[11] Vogel A, Noack J, Hüttman G, et al. Mechanisms of femtosecond laser nanosurgery of cells and tissues [J]. Applied Physics B, 2005, 81(8): 1015-1047.

[12] Kennedy P K, Boppart S A, Hammer D X, et al. A first-order model for computation of laser-induced breakdown thresholds in ocular and aqueous media. II. comparison to experiment[J]. IEEE Journal of Quantum Electronics, 1995, 31(12): 2250-2257.

[13] Feng Q, Moloney J V, Newell A C, et al. Theory and simulation on the threshold of water breakdown induced by focused ultrashort laser pulses[J]. IEEE Journal of Quantum Electronics, 1997, 33(2): 127-137.

[14] Noack J, Vogel A. Laser-induced plasma formation in water at nanosecond to femtosecond time scales: calculation of thresholds, absorption coefficients, and energy density[J]. IEEE Journal of Quantum Electronics, 1999, 35(8): 1156-1167.

[15] Boulais É, Lachaine R, Meunier M. Plasma-mediated nanocavitation and photothermal effects in ultrafast laser irradiation of gold nanorods in water[J]. The Journal of Physical Chemistry C, 2013, 117(18): 9386-9396.

[16] Davletshin Y R, Lombardi A, Cardinal M F, et al. A quantitative study of the environmental effects on the optical response of gold nanorods[J]. ACS Nano, 2012, 6(9): 8183-8193.

[17] Kreibig U, Vollmer M. Experimental methods[M]//

Kreibig U, Vollmer M. Optical properties of metal clusters. Heidelberg: Springer, 1995, 25: 203-274.

[18] Bisker G, Yelin D. Noble-metal nanoparticles and short pulses for nanomanipulations: theoretical analysis [J]. Journal of the Optical Society of America B, 2012, 29(6): 1383.

[19] Hatef A, Meunier M. Plasma-mediated photothermal effects in ultrafast laser irradiation of gold nanoparticle dimers in water [J]. Optics Express, 2015, 23(3): 1967-1980.

[20] Liu X J, Lin Q Y, Tian Y H, et al. Metal-chelate induced nanoparticle aggregation enhanced laser-induced breakdown spectroscopy for ultra-sensitive detection of trace metal ions in liquid samples [J]. Journal of Analytical Atomic Spectrometry, 2020, 35 (1): 188-197.

[21] Simakin A, Astashev M E, Baimler I V, et al. The effect of gold nanoparticle concentration and laser fluence on the laser-induced water decomposition [J]. The Journal of Physical Chemistry B, 2019, 123(8): 1869-1880.

[22] Koral C, Dell'Aglio M, Gaudiuso R, et al. Nanoparticle-enhanced laser induced breakdown spectroscopy for the noninvasive analysis of transparent samples and gemstones [J]. Talanta, 2018, 182: 253-258.

[23] NANOSHEL. Aluminum coated silica nanopowder (Al, < 100 nm, SiO_2 coated, 99.9%) [EB/OL]. [2020-11-23]. https://www.nanoshel.com/product/aluminium-nanoparticle-silica-coating.

[24] Zafar S, Conrad K A, Liu Q, et al. Thickness and effective electron mass measurements for thin silicon dioxide films using tunneling current oscillations [J]. Applied Physics Letters, 1995, 67(7): 1031-1033.

[25] Vogel A, Rockwell B A. Roles of tunneling, multiphoton ionization, and cascade ionization for femtosecond optical breakdown in aqueous media [R]. Lubeck: Lubeck Medical University, 2009.

[26] Sacchi C A. Laser-induced electric breakdown in water [J]. Journal of the Optical Society of America B, 1991, 8(2): 337-345.

[27] Wu A Q, Chowdhury I H, Xu X F. Femtosecond laser absorption in fused silica: numerical and experimental investigation [J]. Physical Review B, 2005, 72(8): 085128.

[28] Docchio F. Lifetimes of plasmas induced in liquids and ocular media by single Nd:YAG laser pulses of different duration [J]. Europhysics Letters (EPL), 1988, 6(5): 407-412.

[29] Hopkins P E, Phinney L M, Serrano J R, et al. Effects of surface roughness and oxide layer on the thermal boundary conductance at aluminum/silicon interfaces [C]//Proceedings of 2010 14th International Heat Transfer Conference, August 8-13, 2010, Washington, DC, USA. New York: ASME, 2011: 313-319.

[30] Hu M, Goicochea J V, Michel B, et al. Thermal rectification at water/functionalized silica interfaces [J]. Applied Physics Letters, 2009, 95 (15): 151903.

[31] Vial A, Laroche T. Description of dispersion properties of metals by means of the critical points model and application to the study of resonant structures using the FDTD method [J]. Journal of Physics D: Applied Physics, 2007, 40(22): 7152-7158.

[32] Vial A, Laroche T. Comparison of gold and silver dispersion laws suitable for FDTD simulations [J]. Applied Physics B, 2008, 93(1): 139-143.

[33] Novo C, Gomez D, Perez-Juste J, et al. Contributions from radiation damping and surface scattering to the linewidth of the longitudinal plasmon band of gold nanorods: a single particle study [J]. Physical Chemistry Chemical Physics, 2006, 8(30): 3540-3546.

[34] Sönnichsen C, Franzl T, Wilk T, et al. Drastic reduction of plasmon damping in gold nanorods [J]. Physical Review Letters, 2002, 88(7): 077402.

[35] Scharte M, Porath R, Ohms T, et al. Do Mie plasmons have a longer lifetime on resonance than off resonance? [J]. Applied Physics B, 2001, 73(4): 305-310.

[36] Boulais É, Lachaine R, Meunier M. Plasma mediated off-resonance plasmonic enhanced ultrafast laser-induced nanocavitation [J]. Nano Letters, 2012, 12 (9): 4763-4769.

[37] Davletshin Y R, Kumaradas J C. The role of morphology and coupling of gold nanoparticles in optical breakdown during picosecond pulse exposures [J]. Beilstein Journal of Nanotechnology, 2016, 7: 869-880.

[38] Lin Z, Zhigilei L V, Celli V. Electron-phonon coupling and electron heat capacity of metals under conditions of strong electron-phonon nonequilibrium [J]. Physical Review B, 2008, 77(7): 075133.

[39] Valette S, le Harzic R, Huot N, et al. 2D calculations of the thermal effects due to femtosecond laser-metal interaction [J]. Applied Surface Science, 2005, 247(1/2/3/4): 238-242.

[40] Keldysh L V. Ionization in the field of a strong electromagnetic wave [J]. Journal of Experimental and Theoretical Physics, 1965, 47(5): 1307-1314.

[41] DeMichelis C. Laser induced gas breakdown: a bibliographical review [J]. IEEE Journal of Quantum

Electronics, 1969, 5(4): 188-202.

[42] Linz N, Freidank S, Liang X X, et al. Wavelength dependence of nanosecond infrared laser-induced breakdown in water: evidence for multiphoton initiation via an intermediate state [J]. Physical Review B, 2015, 91(13): 134114.

[43] Linz N, Freidank S, Liang X X, et al. Wavelength dependence of femtosecond laser-induced breakdown in water and implications for laser surgery [J].

Physical Review B, 2016, 94(2): 024113.

[44] Sudrie L, Couairon A, Franco M, et al. Femtosecond laser-induced damage and filamentary propagation in fused silica [J]. Physical Review Letters, 2002, 89(18): 186601.

[45] Vogel A, Noack J, Nahen K, et al. Energy balance of optical breakdown in water at nanosecond to femtosecond time scales [J]. Applied Physics B, 1999, 68(2): 271-280.

Mechanism of Femtosecond Laser-Induced Breakdown Mediated by Al/SiO₂ Core/Shell Nanostructures

Lin Qing[1,2*], Ren Naifei[2], Song Anran[1], Xia Guangzhi[1]

[1] *School of Mechanical and Electrical Engineering, Suqian College, Suqian, Jiangsu 223800, China;*
[2] *School of Mechanical Engineering, Jiangsu University, Zhenjiang, Jiangsu 212013, China*

Abstract

Objective Physical fields in femtosecond laser-induced water breakdown by Al/SiO₂ core/shell nanostructure were calculated. By the interaction of a femtosecond laser pulse and nanostructures, the near-field of nanostructures along the laser polarization direction was enhanced, which leads to the breakdown of water in the neighborhood. The physical model for the femtosecond laser-induced breakdown includes the electromagnetic field model, two-temperature model, plasma model, and heat transfer model. Calculation of these four physical fields was realized in this paper. Size corrections on the optical properties of the aluminum nanoparticle by modifying the critical point model were considered. This provided more accurate results of dielectric function for aluminum nanoparticles under femtosecond laser irradiation.

Methods This study employed the radio-frequency module, electromagnetic waves, and frequency domain interface of COMSOL to model electromagnetic wave propagation in different media and structures. A two-temperature model for the evolution of the lattice temperature of nanoparticles and the finite heat diffusion at the aluminum-silica-water interface during a femtosecond laser pulse irradiation was solved. It was coupled to the electromagnetic model through the resistive loss during the laser-pulse interaction with nanostructures. The plasma rate equations from the Keldysh theory for multiphoton ionization, the tunneling effect, avalanche ionization, diffusion, and recombination losses were also solved and used to calculate the dynamics of the free-electron plasma density around nanoparticles. The plasma dynamics model was coupled with the electromagnetic model through the electric field value and the change in the dielectric function of water due to the free-electron plasma formation. During the nanoparticle laser-pulse interaction, free-electron plasma generation occurs outside the nanoparticle, whereas a nanoparticle with silica nanoshell, free-electron plasma is generated in silica and water. The morphology of the monomer, dimer, and trimer of nanoparticles with silica shell was investigated. To account for the separation by coupling medium molecules or surfactant on the surface of the particles, assemblies of particles were spaced several nanometers (d_g) apart, keeping a strong plasmonic coupling effect. The structure of aluminum nanoparticles is shown in Fig. 1, with d representing the diameter of a nanoparticle, d_s representing the thickness of the silica shell, and d_g representing the distance between adjacent nanoparticles.

Results and Discussions Near-field enhancement of nanoparticle monomer, dimer and trimer, femtosecond laser breakdown threshold, the evolution of the lattice temperature, and water plasma temperature were considered. The relative electric near-field enhancement, $|E|/E_0$, for different morphologies of Al/SiO₂ core/shell nanoparticles in water (Fig. 4) shows the maximum of the relative electric field enhancement for the monomer was 2.23 times. This was located on both sides of the monomer, along the polarization direction (Z-axis) of the incident laser electric field, as shown in Fig. 4 (a1). That of dimer and trimer was 4.23 times and 4.38 times, respectively, as shown in

Figs. 4 (b1) and (c1). The maximum electric field lies between nanoparticles and is along the polarization direction of the incident laser electric field, as shown in Figs. 4 (b2) and (c2). The maximum electric field of dimer and trimer was doubled compared with the monomer. This indicated that the near-field enhancement of the polymerized Al/SiO$_2$ core/shell nanoparticles was stronger. The extinction cross-sections of monomer, dimer, and trimer at the incident wavelength of 200−600 nm are shown in Fig. 6. The resonance peak was 16735 nm^2 at 230 nm for trimer, 4433 nm^2 at 200 nm for dimer, and 2734 nm^2 at 230 nm for monomer. In this example, the extinction cross-sections of the trimer, dimer, and monomer at incident wavelength $\lambda = 580$ nm were 4115, 209, and 74 nm^2, respectively. These were in the non-resonant state. The evolution of plasma electron density for different morphologies of Al/SiO$_2$ core/shell nanoparticles is shown in Fig. 7. The laser fluence required by plasma electrons to reach the breakdown threshold decreased gradually for monomer, dimer to trimer, due to improvement in the near-field enhancement of nanoparticles. The femtosecond laser breakdown threshold of the pure water was 1428 mJ/cm^2, as with the parameters (wavelength and pulse width) in this paper. This indicated that the Al/SiO$_2$ core/shell nanostructure reduces the required laser intensity. The lattice temperature of different morphologies of Al/SiO$_2$ core/shell nanoparticles at corresponding laser breakdown fluence of $t = 1200$ fs is shown in Fig. 8. Similarly, the evolution of lattice temperature of different morphology of Al/SiO$_2$ core/shell nanoparticles was shown in Fig. 9.

Conclusions　The calculation results showed that Al/SiO$_2$ core/shell nanostructure significantly reduces the water breakdown threshold of the femtosecond laser. Also, the near-field enhancement of polymeric nanoparticles was stronger than that of the monomer. Furthermore, the lattice temperature of monomer was higher than the melting point, while that of dimer and trimer was lower. In sum, polymeric Al/SiO$_2$ core/shell nanostructures are endowed with great potential for applications in fields such as femtosecond laser-induced cavitation in water and cell transfection, among others.

Key words　laser technology; laser-induced breakdown; aluminum nanostructures; interaction mechanism; coupling of multiple physical fields

OCIS codes　140.3440; 160.4236; 350.5400